Journal of Materials Chemistry A

Accepted Manuscript

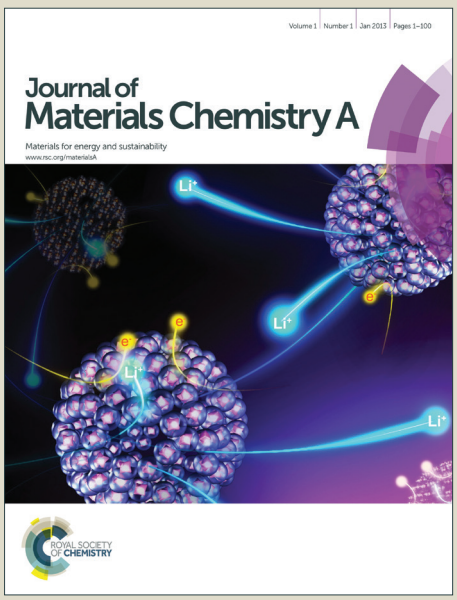

ROYAL SOCIETY OF CHEMISTRY

www.rsc.org/materialsA

Cite this: DOI: 10.1039/c0xx00000x

www.rsc.org/xxxxxx

ARTICLE TYPE

Black Nanostructured Nb_2O_5 with Improved Solar Absorption and Enhanced Photoelectrochemical Water Splitting

Houlei Cui,[a] Guilian Zhu,[a] Yian Xie,[a] Wei Zhao,[a] Chongyin Yang,[a] Tianquan Lin,[a] Hui Gu[a] and Fuqiang Huang*[a,b]

Received (in XXX, XXX) Xth XXXXXXXXX 20XX, Accepted Xth XXXXXXXXX 20XX
DOI: 10.1039/b000000x

Black TiO_2, with increased solar light absorption and enhanced photocatalytic and photoelectrochemical (PEC) performance, has attracted enormous attention, stimulating us to explore the blackening of other oxide semiconductors for enhanced properties. Here, we report the fabrication of black nanostructured Nb_2O_5 and its enhanced PEC property for the first time. We successfully prepare oxygen-deficient black Nb_2O_5 nanochannels, which contain considerable amount of oxygen vacancies (Nb^{4+} sites) serving as shallow donors. The black Nb_2O_5 exhibits strong visible and infrared light absorption, which can absorb 75.5% solar energy superior to 5.7% for pristine Nb_2O_5. The PEC performance of black Nb_2O_5 photoanode is significantly enhanced with a relatively large photocurrent of 1.02 mA cm^{-2} and high applied bias photon-to-current efficiency (ABPE) of 0.345%, in comparison with the poor performance of pristine Nb_2O_5 (0.084 mA cm^{-2} photocurrent and 0.056% ABPE). These results indicate that black Nb_2O_5 is a promising material for PEC application and solar energy utilization.

Introduction

Black TiO_2 firstly prepared in 2011 by high H_2-pressure process exhibited remarkable solar light absorption and photocatalytic hydrogen production performance.[1] Afterwards, a series of follow-up investigations were triggered to explore the fabrication and mechanism of black TiO_2.[2-6] Black TiO_2 fabricated by various methods, such as H_2 annealing,[2,3] H_2 plasma treatment[4] and aluminium reduction,[5,6] generally comprises surface disorders and oxygen vacancies, and yields increased photocatalytic and/or photoelectrochemical (PEC) performance. This motivates us to explore the blackening of other oxide semiconductors for enhanced solar absorption and PEC water splitting. Beyond TiO_2 known as the most common material for PEC applications, many other semiconductor metal oxides (ZnO,[7] WO_3,[8] α-Fe_2O_3,[9] $BiVO_4$,[10] etc.), have also been extensively studied for PEC water splitting and delivered different PEC performances.

However, niobium pentoxide (Nb_2O_5), one of the most important n-type semiconductor materials, has barely been reported for PEC application in the past years. Nb_2O_5 has a wide band gap (E_g) of 3.1~4.0 eV,[11-14] similar to TiO_2 and ZnO, with a conduction band comprised of empty Nb^{5+} 4d orbitals.[15] It has been widely investigated for various applications, such as electrochromism devices, microelectronics, lithium-ion batteries, solar cells and photocatalyst.[16-20] To date, many Nb_2O_5 nanostructures, including nanoparticles, nanobelts, nanowires, nanorods and nanoforests, have been synthesized by hydrothermal, electrospinning, pulsed laser deposition and so on.[21-25] Recently, highly ordered Nb_2O_5 nanochannels have been fabricated by electrochemical anodic oxidation in a glycerol based electrolyte,[26] and been utilized as photoanodes for dye-sensitized solar cells (with photovoltaic efficiency of 4.48%).[27] Though the band edge potentials of Nb_2O_5 straddle the hydrogen and oxygen redox potentials as reported,[12,14,28] and it exhibits some activity for photocatalytic hydrogen production,[29] the PEC performance of Nb_2O_5 has barely been reported in the past years. Consequently, the usage of Nb_2O_5 photoanodes for PEC water splitting is worth researching.

In this work, we prepared highly ordered oxygen-deficient black Nb_2O_5 nanochannels by aluminium reduction of pristine Nb_2O_5 nanochannels for the first time. The substantial oxygen vacancies (Nb^{4+} sites) in the black Nb_2O_5 nanochannels improve solar absorption up to 75.5%. The black Nb_2O_5 nanochannels photoanode exhibited an excellent PEC performance due to the improved charge transport and separation and the slightly extended visible light response. In comparison with pristine Nb_2O_5, black Nb_2O_5 nanochannels showed an order of magnitude enhanced photocurrent density and reasonable stability.

Experimental

Materials

Nb foils (99.7%, 127 μm in thickness) were purchased from Alfa Aesar. K_2HPO_4 and glycerol were purchased from Sinopharm Chemical Reagent Co. Ltd, China. Aluminium powder (99.9%, 200-300 mesh) was purchased from Aladdin Industrial Inc., China.

Electrochemical Anodization to Prepare Amorphous Nb_2O_5 Nanochannels

Niobium foils with dimension of 2.0 cm × 1.0 cm were cleaned by sonication in soap solution, acetone, ethanol and deionized water successively. Then the foils were chemically polished in a mixture of $HF/HNO_3/H_2O$ (1:4:5) for 10 minutes to obtain smooth surface. Finally, the samples were dried by nitrogen gas.

The anodization was conducted in the anhydrous glycerol electrolyte containing 10 wt% K_2HPO_4. Prior to anodization, the electrolyte was held at 180 °C for 4 h to reduce the water content. The target area for anodization was set as 1.0 cm × 1.0 cm on single side of the Nb foil, and the undesired part was protected by insulating tape. The samples were anodized at 20 V supplied by a DC power supply (INTERLOCK IPD-20001SLU, China) for 5 minutes, at 180 °C as suggested previously, to produce ~6.2 μm thick Nb_2O_5 nanochannels. Anodization was carried out in a two-electrode system configuration with a Pt plate as the cathode electrode.

Preparation of Pristine and Black Nb_2O_5 Nanochannels

The as-anodized samples were rinsed thoroughly with deionized water and ethanol, and spontaneously dried in the air for several hours. Then they were preliminarily crystallized in ambient air at 450°C for 30 minutes (ramp up/down of 6 °C/minute) to remove the residual glycerol and to obtain stoichiometric Nb_2O_5 nanochannels (TT phase). After cooling down, the samples were then annealed at a higher temperature of 600 °C for 4 h in Ar atmosphere and aluminium reduction device, respectively, to acquire quasi-stoichiometric pristine Nb_2O_5 nanochannels (T phase) and oxygen-deficient black Nb_2O_5 nanochannels (T phase). Ar was mainly used for protect the Nb foil from being oxidize into Nb_2O_5 powder at such a relatively high temperature. When conducting aluminium reduction process, Nb_2O_5 nanochannels and aluminium powder were placed separately in a two-zone tube furnace and then evacuated to a base pressure below 8 Pa. Subsequently, the Nb_2O_5 samples and aluminium powder were heated to 600 °C and 800 °C, respectively.

Material Characterization

To investigate the microstructure and composition of the samples, UV-Vis-NIR spectrometer (Hitachi U4100), field emission scanning electron microscopy (FE-SEM, Hitachi S-4800), transmission electron microscopy (TEM, JEOL JEM-2100F), X-ray diffraction (XRD, Bruker D8 Advance), X-ray photoelectron spectroscopy (XPS, PHI 5000C ESCA System) with Mg K_α X-ray ($h\nu$ = 1253.6 eV) at 14 kV and Raman spectroscopy (Thermal Dispersive Spectrometer) with 532 nm laser excitation were employed. PL spectra were measured at 300 K on a spectrofluorometer (FluoroMax-4, HORIBA Jobin Yvon) with an excitation wavelength of 310 nm. To calculate the amount of solar absorption (AM 1.5G), we firstly get a new ordinate (absorbance × light intensity) as a function of wavelength, then compute the integrals within different wavelength range (200-400 nm for UV-light, 400-760 nm for Vis-light, and 760-2400 nm for NIR-light). Dividing the integrals by the total solar energy (integral from 200-2400 nm of AM 1.5G), the percentages presented in Table 1 are acquired.

Characterization of Photoelectrochemical Performance of the Samples

To characterize the photoelectrochemical performance of the samples, a conventional three-electrode system was utilized to conduct electrochemical measurements with an electrochemical workstation (CHI660B, CH Instruments). The Nb_2O_5 nanochannels attached on Nb substrates were used directly as the working electrode, with a Pt wire and an Ag/AgCl (KCl saturated) electrode as counter and reference electrodes respectively in 1 M NaOH aqueous solution (pH = 13.6). A set of linear sweeps and transient photocurrent responses were recorded in the dark and under illumination. A 150W Xe lamp was used as the light source to simulate the sunlight irradiation. The light intensity was measured by a calibrated Si photodiode. Mott-Schottky plots were derived from impedance-potential tests conducted at a frequency of 100 Hz in the dark. Nyquist plots were acquired from AC impedance tests performed over a frequency range of 0.01 Hz to 100 kHz at an open-circuit voltage under illumination with an amplitude of 5 mV. The IPCE was measured using a 300 W Xe lamp and a monochromator (Oriel Cornerstone 130 1/8 m). The visible light was obtained by excluding the UV part of the simulated sunlight with a 420 nm cutoff glass light filter. Stability test was carried out under 100 mW cm^{-2} illumination at 0.23 V for 3 hours to record the photocurrent decay.

Results and discussion

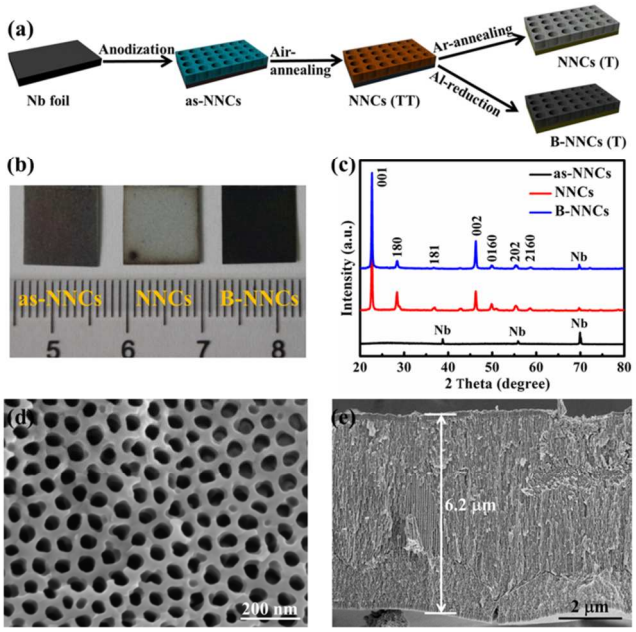

Fig. 1 (a) Schematic fabrication of Nb_2O_5 nanochannels. (b) Photographs of the as-NNCs, NNCs, and B-NNCs. (c) XRD patterns of three samples. (d) Typical top view and (e) side view FE-SEM images of B-NNCs.

The preparation of highly ordered pristine and black Nb_2O_5 nanochannels mainly comprises three procedures, as schematically illustrated in Fig. 1a. Firstly, the cleaned and chemically polished Nb foil was electrochemically anodized in an anhydrous glycerol solution containing 10 wt% K_2HPO_4 at an elevated temperature to fabricate amorphous Nb_2O_5 nanochannels (denoted as as-NNCs), by reference to previous report[26] with some modification. Subsequently, the as-NNCs were calcined in air at 450 °C for 30 min to remove the residual glycerol and to obtain stoichiometric TT-phase (pseudohexagonal) Nb_2O_5 nanochannels, which are quite thermodynamically unstable.[30]

Finally, pristine T-phase (orthorhombic) Nb_2O_5 nanochannels (NNCs) or the black specimen (B-NNCs) were achieved by further processing TT-phase sample with annealing in Ar atmosphere or aluminium reduction treatment at 600 °C for 4h, respectively. It is noteworthy that Ar gas was used to protect the Nb foil substrate from being oxidized by O_2 into Nb_2O_5 powder at relatively high temperature. The details about the aluminium reduction device and mechanism were clearly described in our previous report.[5] As shown in Fig. 1b, NNCs and B-NNCs on Nb substrates present white and black color respectively. Excluding the influence of Nb substrates, the color difference of white and black is more distinct for NNCs and B-NNCs powder (Fig. S1, ESI†).

The phase evolution of three samples with different annealing treatments was studied by using powder XRD patterns, as presented in Fig. 1c. Only the peaks of Nb substrates are observed for as-NNCs, verifying their amorphous feature. The sharp reflections of NNCs are well indexed as (001), (180), (181), (002), (0160), (202), and (2160) planes of orthorhombic Nb2O5 (T-Nb_2O_5, JCPDS No. 30-0873). No diffraction peaks arising from impurities such as TT-Nb_2O_5, M-Nb_2O_5 (tetragonal) and NbO_2 are detected, indicating the high purity of the sample. As with NNCs, the B-NNCs sample also comprises two phases of T-Nb_2O_5 and Nb, indicated from its XRD pattern. The peak positions of B-NNCs are almost unchanged, compared with the corresponding peaks of NNCs, indicating the identical interplanar distances of orthorhombic Nb_2O_5 in NNCs and B-NNCs. However, there is a noticeable change in the intensity ratios of different peaks, such as (180) and (002), which may be induced by the crystal orientation growth during the aluminium reduction process.

Field emission scanning microscopy (FE-SEM) was used to investigate the morphology of B-NNCs. Fig. 1d is the top view of B-NNCs on Nb foil substrate. It is clearly seen that the uniform Nb_2O_5 nanochannels are vertically arranged in order on the surface of Nb foil. The inner diameters and wall thicknesses of the nanochannels are about 40~50 nm and 20~30 nm, respectively. Cross sectional SEM image shown in Fig. 1e reveals that the nanochannelled film comprises different sets of nanochannelled structure, possessing a whole thickness of about 6.2 μm. A barrier layer with a thickness of about 150 to 200 nm, which is a characteristic of nano-structured films prepared by electrochemical anodization, can also be observed underneath the nanochannels (top of the side view). The morphology and structure of the sample were further examined by TEM (Fig. S2, ESI†). The nanochannels appear ordered, straight but unsmooth feature, comprising many disintegrated particles. Well-resolved lattice fringes of 0.392 nm observed from the HRTEM image of nanoparticles derived from the wall of B-NNCs, coincide with the (001) plane of T-Nb_2O_5 (JCPDS No.30-0873), demonstrating the orthorhombic Nb_2O_5 phase again.

The absorption spectra of NNCs and B-NNCs are shown in Fig. 2. NNCs sample exhibits a sharp absorption edge around 400 nm and merely responds to UV region, corresponding to the electronic transition from the valence band to the conduction band of Nb_2O_5. However, B-NNCs sample which delivers nearly an overlapped absorbance with NNCs in the UV light region, shows a dramatically enhanced light absorption from visible (Vis) light to infrared (IR) light region. The improved Vis-IR light absorption can be ascribed to the additional transitions caused by increased Nb^{4+} states, oxygen vacancies and other defects at different energy levels.[5,31,32] The optical band gaps deduced from Tauc plots (Fig. S3, ESI†) constructed from the absorption spectra are 3.19 and 3.07 eV for NNCs and B-NNCs, respectively. This decrease in the band gap of B-NNCs is consistent with the assumption that an electronic band is located just below the conduction band of pristine Nb_2O_5.

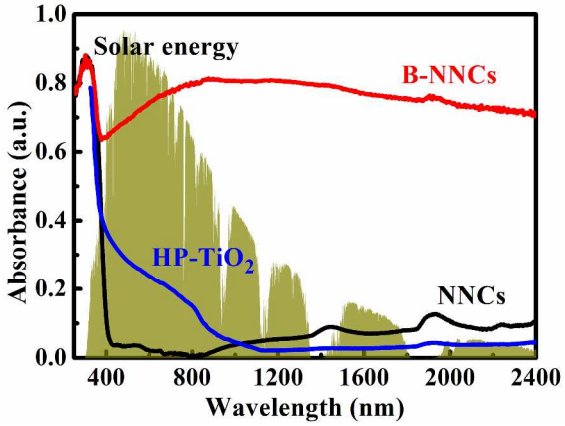

Fig. 2 Absorption spectra of the NNCs and B-NNCs, in comparison with the high-pressure hydrogenated black titania (HP-TiO_2, from Ref. 1).

Based on our calculation of the solar absorption in different spectrum region (Table 1), the pristine Nb_2O_5 (NNCs) possesses little absorption in visible and infrared light regions. As a consequence, its total solar absorption amount is merely 5.7%, which means an inefficient utilization of the solar energy. In contrast, the total solar absorption of black Nb_2O_5 (B-NNCs) reaches up to 75.5%, with significantly increased Vis-light absorption (36.8%) and IR-light absorption (35.4%). In addition, the famous high-pressure hydrogenated black titania (HP-TiO_2, data from Ref. 1) has a much weaker absorption both in the IR-light region (2.8%) and Vis-light region (13.2%), with a total solar absorption about 18.2%.

X-ray photoelectron spectroscopy (XPS) was performed to investigate the difference of the surface bonding of the NNCs and B-NNCs. The Nb $3d_{5/2}$ and $3d_{3/2}$ XPS peaks in the NNCs are centered at binding energy of 207.2 and 210.0 eV, as shown in Fig. 3a, which is typical for the Nb^{5+}-O bonds in Nb_2O_5. In comparison, additional small peaks centering separately at 205.8 eV and 208.3 eV could be extracted out from the Nb 3*d* XPS of B-NNCs, which conform to the $3d_{5/2}$ and $3d_{3/2}$ XPS peaks of Nb^{4+}.[33-35] The emerging Nb^{4+} signals suggest that oxygen vacancies are introduced into the B-NNCs during the aluminium reduction process. As Nb_2O_5 is a common electrochromic material, the reduction of Nb^{5+} to lower valence state Nb^{4+} could induce the coloration from transparent to brown, grey or blue.[36,37] The oxygen-deficient B-NNCs comprise considerable amount of oxygen vacancies, which give rise to the local states below the conduction band edge.[38] In addition, the electrons left in the oxygen vacancies can also interact with adjacent Nb^{5+} to generate the Nb^{4+} species.[38] The Nb^{4+} defects can form a shallow donor level just below the conduction band, which could also contribute to the visible light response. Thus, we deem that the black color

Table 1 Solar absorption, carrier density (N_d), photocurrent (I) of NNCs and B-NNCs.

Sample	total	UV[a]	Vis[b]	IR[c]	N_d (cm^{-3})	I (mA cm^{-2})
solar spectrum	100%	4.7%	50.7%	44.6%	–	–
pristine Nb_2O_5	5.7%	2.5%	1.4%	2.8%	4.64×10^{19}	1.02
black Nb_2O_5	75.5%	3.3%	36.8%	35.4%	2.33×10^{21}	0.084
HP-TiO_2[1]	17.9%	2.3%	12.8%	2.8%	–	–

[a] UV light: < 400 nm; [b] visible light: 400-760 nm; [c] infrared light: > 760 nm.

of B-NNCs derives from the defect states in the band gap, and the intervalence charge transition from Nb^{5+} to Nb^{4+}.

The normalized XPS O 1*s* spectra collected from NNCs and B-NNCs are almost the same (Fig. S4, ESI†), with a single peak at 530.2 eV assigned to the Nb-O bonds, indicating the similar coordination polyhedron of oxygen for each Nb. The valence band spectra of the NNCs and B-NNCs are shown in Fig. 3b. The valence band maxima are estimated by linear extrapolation of the peaks to the baselines, which derives an identical band edge position of 2.96 eV for NNCs and B-NNCs below the Fermi energy, demonstrating a negligible effect of aluminium reduction treatment on the valence band position at the surface of Nb_2O_5 nanochannels. The full XPS spectrum (Fig. S5, ESI†) also reveals that trace amounts of both potassium (K 2*p*) and phosphorus (P 2*p*) can be detected, deriving from K_2HPO_3 in the residual electrolyte. Their effect on the optical and photoelectrochemical properties of the sample should be negligible, for they inevitably exist in all samples.

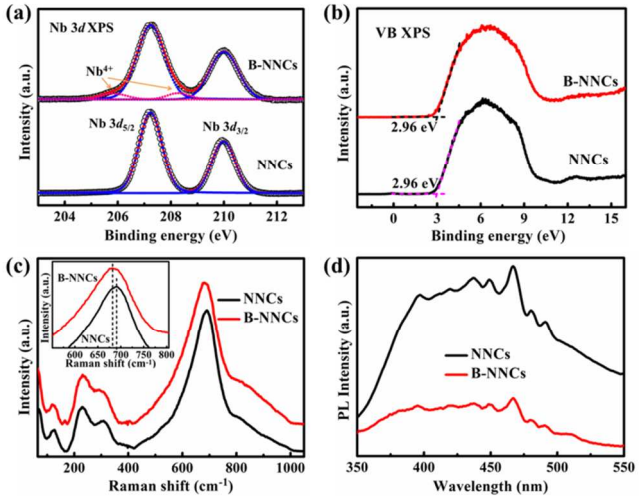

Fig. 3 (a) Nb 3*d* XPS spectra of NNCs and B-NNCs. The black circles are the experimental data, which can be decomposed into a superposition of two fitting curves of Nb^{5+} (shown in blue) and Nb^{4+} (shown in pink). The red curve is the summation of the two decomposed curves. (b) XPS valence band spectra of NNCs and B-NNCs. (c) Raman spectra of NNCs and B-NNCs, inset is the magnification of the TO mode. (d) Photoluminescence emission spectra.

The change of the chemical coordination structure of different samples is unambiguously supported by Raman spectroscopy (Fig. 3c). The Raman spectra of both samples mainly contain five well-defined bands of T-Nb_2O_5, located at ~810 cm^{-1}, ~690 cm^{-1}, ~310 cm^{-1}, ~230 cm^{-1}, and ~120 cm^{-1}, assigned to the LO, TO, T_{2u}, T_{2u}, and lattice vibration mode of T-Nb_2O_5,[38,39] respectively. The strongest symmetric Nb-O stretching mode (TO) of the niobium oxide polyhedra, is associated with the bond order of the niobia polyhedra and structure order.[39] As can be observed, the TO peak of B-NNCs becomes broader, and has a red shift to 682.1 cm^{-1} from 691.2 cm^{-1}, compared with that of NNCs. This should be attributed to the disorder caused by the increased amount of oxygen vacancies in the B-NNCs.

To monitor the behaviour of light-excited electrons and holes in the samples, photoluminescence emission (PL) was measured since it could reflect the separation/recombination of free carriers to some extent. The PL spectra (excited at 310 nm) of the NNCs and the B-NNCs are shown in Fig. 3d. In the wavelength range from 390 nm to 500 nm, both samples display several peaks at the same position. Similar with that of TiO_2, the first peak at 397 nm is ascribed to the emission of bandgap transition, and the others should be attributed to band edge free exciton, bound exciton, and surface defects respectively.[6,31] It is evident that the PL intensity of the B-NNCs sample is lower than that of the NNCs, indicating a relatively low recombination rate of electrons and holes under UV light irradiation owing to increased oxygen vacancies serving as electron traps,[40] which favours high photoelectrochemical activity. Moreover, the additional broad peak around 510 nm might originate from oxygen vacancies in the B-NNCs.[31]

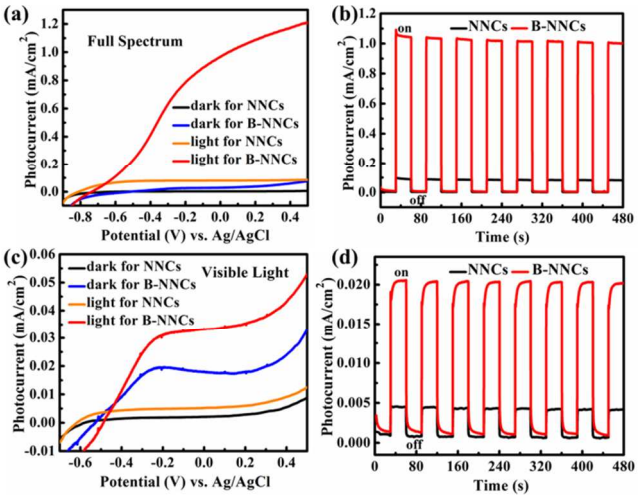

Fig. 4 (a) Linear sweep voltammograms collected under 100 mW cm^{-2} illumination using a three electrodes setup in 1 M NaOH electrolyte (pH = 13.6). (b) Transient photocurrent responses of the samples at 0.23 V vs. Ag/AgCl under full spectrum. (c) Linear sweep voltammograms and (d) transient photocurrent responses collected under visible light (>420 nm).

To investigate the PEC properties of NNCs and B-NNCs, a set of linear sweeps was recorded in the dark, and under 100 mW cm^{-2} illumination, as shown in Fig. 4a. The potential was swept linearly at a scan rate of 10 mV s^{-1} between –0.9 and 0.5 V vs.

Ag/AgCl in 1 M NaOH electrolyte (pH = 13.6). Both photoelectrodes show very low dark current relative to their photocurrent, indicating that no drastic electrocatalytic water splitting occurs. Obviously, the photocurrent of B-NNCs under illumination is distinctly higher than that of NNCs. The onset potential of photocurrent reveals a positive shift from –0.81 V (vs. Ag/AgCl) for NNCs to –0.74 V for B-NNCs, probably due to the slightly limited water oxidation kinetics caused by the increased surface trapping states in B-NNCs.[41,42] After all, more efficient charge separation and transport in the B-NNCs could be confirmed by the significantly higher photocurrent density. It is worth noting that the photocurrent under visible light (> 420 nm) of B-NNCs is also obviously higher than that of NNCs, yet the dark current for B-NNCs shows a significant increase as well, as seen from Fig. 4c. The greatly enhanced electrical conductivity of B-NNCs induced by the increased carrier density, coupled with the massive defect states in B-NNCs, accounts for the distinct increase of dark current. The improved photocurrent under visible light should be attributed to the enhanced visible light absorption of B-NNCs which is mainly caused by the increased amount of oxygen vacancy donor sites, and this improvement will contribute to the overall PEC performance of B-NNCs more or less.

To investigate the photoresponses of NNCs and B-NNCs, the PEC measurement was carried out under illumination with several 60 s light on/off cycles at 0.23 V. The plots of the transient photocurrent responses vs. time under full spectrum are shown in Fig. 4b. Both samples have good photoresponses in chopped light cycles. Without illumination, the current values are almost zero while the photocurrent rapidly rises to a steady-state value upon illumination, which is reproducible for several on/off cycles with almost the identical photocurrent and dark current. The observed steady-state photocurrent of B-NNCs (1.02 mA cm^{-2}) is nearly 12.1 times higher than that of NNCs (0.084 mA cm^{-2}), indicating the larger amount of photo-generated carriers in B-NNCs owing to the improved charge separation and their more efficient transport process from the wall of B-NNCs to the Nb foil substrate. The increased photocurrent and good photoresponse of B-NNCs can also be observed from the chopped linear sweep voltammograms (Fig. S6, ESI†). The transient photocurrent responses to visible light of NNCs and B-NNCs are also measured (Fig. 4d). Upon visible light illumination, the photocurrent of NNCs rapidly rises to a steady-state value, while the rise of the photocurrent of B-NNCs to the steady-state level comprises an instantaneous process and a gradual growth. The observed steady-state photocurrent of B-NNCs (0.02 mA cm^{-2}) is nearly 5 times higher than that of NNCs (0.004 mA cm^{-2}), indicating the larger amount of photo-induced carriers in B-NNCs under visible light owing to the expanded light absorption and photoresponse.

Electrochemical impedance spectroscopy (EIS) provides a powerful method for the study of charge transfer and recombination processes at semiconductor-electrolyte interfaces. Typical Nyquist plots under illumination with frequencies ranging from 0.01 to 100 KHz are shown in Fig. 5a. Both Nyquist plots present explicit arcs, the radius of which is associated directly with the charge-transfer process. Obviously, the B-NNCs photoanode delivers a smaller arc than NNCs, indicating a more efficient interfacial charge transfer and a more effective separation of the photo-generated electron-hole pairs.[43,44]

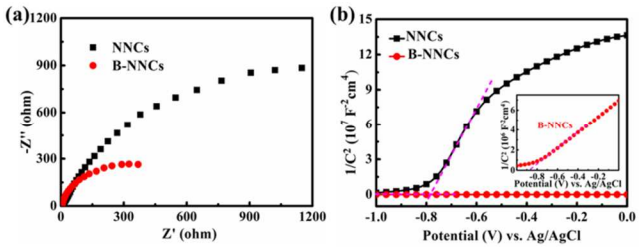

Fig. 5 (a) Nyquist plots of NNCs and B-NNCs photoanode collected at open-circuit potential in 1.0 M NaOH solutions under illumination. (b) Mott–Schottky plots of NNCs and B-NNCs collected at a frequency of 100 Hz.

Mott-Schottky plots were measured at 100 Hz with a 5 mV amplitude in 1.0 M NaOH solutions without illumination, to further explore the information about carrier density and flat-band potential of the samples. The positive slope of Mott-Schottky curves (Fig. 5b) in both samples indicates n-type character of Nb_2O_5 nanochannels. The huge difference of slope of the linear parts in the two plots indicates a tremendous disparity of donor densities in NNCs and B-NNCs. The following equation can be used to calculate the carrier density of semiconductor materials from the slope of Mott-Schottky plots:[45]

$$N_d = (2/e_0\varepsilon\varepsilon_0)[d(1/C^2)/dV]^{-1} \quad (1)$$

where e_0, ε, ε_0, N_d, $d(1/C^2)/dV$ represent the electron charge, the relative dielectric constant of Nb_2O_5 (77 for T-Nb_2O_5),[30] the permittivity of vacuum, the donor density and the straight slope, respectively. The calculated electron densities of NNCs and B-NNCs are separately 4.64×10^{19} and 2.33×10^{21} cm^{-3}. This result confirms that the aluminium reduction process induces a dramatic increase (about 50 times) of electron density, due to the introduction of substantial oxygen vacancies which serve as shallow donors. Thus the electrical conductivity as well as charge transport in B-NNCs will be greatly enhanced. Meanwhile, the increased electron density is expected to shift the Fermi level (E_F) of Nb_2O_5 toward the conduction band, which leads to a larger degree of band bending at the surface of the B-NNCs, and facilitates the charge separation at the interface of the B-NNCs and electrolyte.[2,6] The flat-potentials (E_{fb}), as calculated from the x intercepts of the linear region, are found to be –0.785 and –0.871 V for NNCs and B-NNCs, respectively. As an inherent property of the semiconductor, E_{fb} equals E_F for n-type semiconductor,[46] thus the negative shift of E_{fb} conforms to the upward Fermi level of B-NNCs, which is favorable for water splitting reaction. A proposed energy diagram of NNCs and B-NNCs is given (Fig. S7, ESI†), which schematically illustrates the band-gap narrowing, upward Fermi level and oxygen vacancy states for B-NNCs.

To gain further insight into the charge-transport properties of NNCs and B-NNCs photoanodes, open-circuit photovoltage (V_{oc}) decay (OCPVD) measurement was conducted to assess photo-generated electron lifetime and thus to evaluate the recombination rate of the photo-generated electrons and holes. Turning off illumination at a steady state and examining the subsequent decay of photovoltage constitute the OPCVD test. As can be observed from Fig. 6a, the V_{oc} of both photoanodes exhibits a negative shift

under illumination compared to that in the dark, for the photo-generated electrons accumulate inside the nanochannels, and rapidly shift the Fermi level to more cathodic potentials. Once turning off the illumination, the accumulated electrons will be redistributed due to charge recombination until the Fermi level of photoanodes reaches a new level, resulting in the gradual V_{oc} decay to the original level. It can be seen that the V_{oc} decay rate of B-NNCs photoanode is apparently slower than that of NNCs, demonstrating moderate recombination kinetic in B-NNCs.

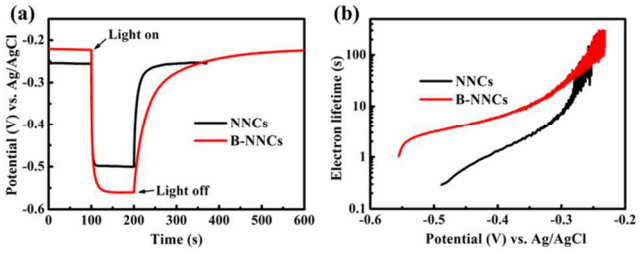

Fig. 6 (a) Open circuit potential vs. time profile of NNCs and B-NNCs photoanodes. (b) Electron lifetime determined from the decay of open circuit potential after light off.

Lifetime of photo-generated electrons can be calculated from the V_{oc} decay rate by the following equation:[47]

$$\tau_n = (k_B T/e)/\mathrm{d}(V_{oc}/\mathrm{d}t)^{-1} \quad (2)$$

where τ_n is the potential dependent electron lifetime, k_B is Boltzmann constant, T is the temperature (about 300 K), e is the charge of a single electron, and V_{oc} is the open-circuit voltage at time t. The calculated electron lifetime is shown in Fig. 6b as a function of V_{oc}. As expected, B-NNCs photoanode displays a prolonged electron lifetime relative to that of NNCs at the same potential, which might be ascribed to the increased oxygen vacancies serving as electron traps and other surface adsorption sites.[40,48] This is consistent with the PL result and contributes to better charge-transport and photoelectrochemical performance.

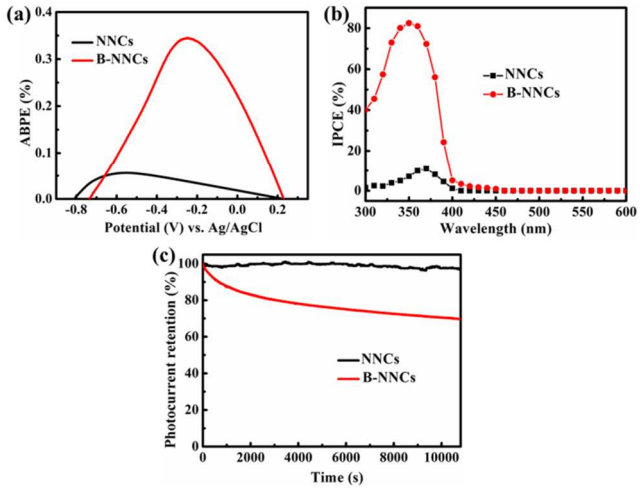

Fig. 7 (a) ABPE of the NNCs and B-NNCs as a function of applied potential. (b) IPCE spectra in the region of 300-600 nm at 0.23 V vs. Ag/AgCl. (c)Photocurrent stability of NNCs and B-NNCs collected under 100 mW cm^{-2} illumination at 0.23 V vs. Ag/AgCl.

Applied bias photon-to-current efficiency (ABPE) is an important figure of merit to measure the PEC water splitting performance of a semiconductor photoanode, which can represent the solar-to-hydrogen (STH) efficiency more or less. Assuming 100% Faradaic efficiency, the ABPE of photoanodes can be calculated from the 3-electrode photocurrent-potential plots using the equation:[49]

$$\mathrm{ABPE}(\%) = I(1.23 - V_{RHE})/J_{light} \quad (3)$$

where V_{RHE} is the applied bias vs. RHE ($V_{RHE} = V_{Ag/AgCl} + 0.197 + 0.0591 \times \mathrm{pH}$),[48] I is photocurrent density at the measured bias, and J_{light} is the irradiance intensity of 100 mW cm^{-2}. Fig. 7a presents the ABPE of NNCs and B-NNCs as a function of $V_{Ag/AgCl}$. The NNCs photoanode delivers a maximum ABPE of 0.056% at –0.554 V (vs. Ag/AgCl), while the B-NNCs sample achieves a distinctly higher maximum ABPE of 0.345% at a higher bias of –0.247 V. In addition, the 2-electrode system can reflect the practical PEC performance of photoanode more realistically. Thus we measured the 2-electrode (working electrode and Pt counter electrode) photocurrent-potential curves and calculated the corresponding ABPE (Fig. S8, ESI†). The overall shape and numerical level of 2-electrode *J-V* curves are quite analogous to that of 3-electrode. The maximum ABPEs obtained from the 2-electrode *J-V* curves are 0.06% at 0.40 V (vs. Pt) for NNCs, and 0.30% at 0.77 V for B-NNCs, respectively.

In order to understand the interplay between the photoactivity and the light absorption of two types of nanochannels, incident-photon-to-current-conversion efficiency (IPCE) measurements were performed on NNCs and B-NNCs photoanodes at 0.23 V (vs. Ag/AgCl) (Fig. 7b). The IPCE can be expressed by the equation:[50]

$$\mathrm{IPCE}(\%) = (1240\,I)/\lambda J_{light} \quad (4)$$

where I is the measured photocurrent density at a specific wavelength, λ is the wavelength of incident light, and J_{light} is the measured irradiance at a specific wavelength. In comparison with NNCs, the B-NNCs photoanode exhibits greatly enhanced photoactivity over the entire UV region and achieves IPCE values around 60% in the wavelength range from 300 to 380 nm (Fig. 7b). Maximum IPCE of 82.5% is acquired at 350 nm for B-NNCs, while the highest IPCE is merely 10.9% at 370 nm for NNCs. This result indicates that the UV light is effectively used for PEC water splitting by B-NNCs, in which the separation and transport of photo-generated carriers are more efficient. Moreover, the photoresponse range of B-NNCs extends to visible light, supported by the slightly increased IPCE from 400 nm to 450 nm, and this agrees well with the extended absorption in the absorption spectrum and the increased photocurrent under visible light. The integrated photocurrent based on the IPCE data has also been shown in the ESI (Fig. S9†), which reaches 0.838 mA cm^{-2} for B-NNCs and is similar to the PEC measurement. According to the integration, the visible light response (>420 nm, 0.019 mA cm^{-2}) contributes 2.27% of the total AM 1.5 G photocurrent, which is a fairly small part mainly due to the photoelectrochemically inactive transition from the valence band to aluminum reduction induced oxygen vacancy states. Therefore, the enhanced photoresponse in UV region accounts for the vast part of the overall PEC performance of B-NNCs, and the contribution from the visible light photoresponse is very limited.

Long-term stability is one of the key criteria for the practical PEC applications, for photoanodes generally suffer from photocorrosion in aqueous electrolytes.[51] In order to examine the stability of the samples, the photocurrent decay under 100 mW cm^{-2} illumination at 0.23 V was monitored (Fig. 7c). Throughout the test, photocurrent of NNCs photoanode keeps almost unchanged at the quite low level. In contrast, the photocurrent of B-NNCs drops about 16% within the first half-hour, and then declines gradually to 69.7% of the initial value after 3 hours. The photocurrent decay should mainly derive from the irreversible electrochemical oxidation of the reduced-state B-NNCs in the presence of water and oxygen. After all, the 69.7% retention suggests a reasonable stability, and better stability might be expected to achieve by coating of passivation layer.

Conclusions

In summary, oxygen-deficient black Nb_2O_5 nanochannels have been successfully prepared via electrochemical anodization, air-annealing, and aluminium reduction treatment successively. The aluminium reduction technique is demonstrated to be an effective method to modify the Nb_2O_5 nanochannels, by introducing considerable amount of oxygen vacancies (Nb^{4+} sites), which serve as shallow donors. The obtained black Nb_2O_5 nanochannels exhibit dramatically enhanced Vis-IR light absorption, increased carrier density and electrical conductivity. Benefitting from improved charge transport and charge separation, the oxygen-deficient black Nb_2O_5 nanochannels photoanode delivers much more efficient photoelectrochemical water-splitting performance than pristine NNCs. A relatively large photocurrent of 1.02 mA cm^{-2} and high ABPE of 0.345% can be obtained from B-NNCs, significantly superior to the poor performance of NNCs (0.084 mA cm^{-2} photocurrent, and 0.056% ABPE). Reasonable photocurrent stability is confirmed by the 69.7% retention of initial value after 3 hours illumination. As far as we know, this is the first time for the study and modification of Nb_2O_5 materials for PEC application. Our study shows that Nb_2O_5 could be promising PEC photoanode material after proper modification, and "blackening" could be a promising method to modify other semiconductors for enhanced properties.

Acknowledgements

This work was financially supported by NSF of China (Grants 91122034, 51125006, 61376056, and 51402336), and Science and Technology Commission of Shanghai (Grants 13JC1405700 and 14YF1406500).

Notes and references

[a] *State Key Laboratory of High Performance Ceramics and Superfine Microstructure and CAS Key Laboratory of Materials for Energy Conversion, Shanghai Institute of Ceramics, Chinese Academy of Sciences, Shanghai 200050, P.R. China. E-mail: huangfq@mail.sic.ac.cn*

[b] *Beijing National Laboratory for Molecular Sciences, College of Chemistry and Molecular Engineering, Peking University, Beijing 100871, P.R. China*

† Electronic Supplementary Information (ESI) available: [Photographs, TEM images, Tauc plots, O 1*s* spectra, XPS survey spectrum, Schematic energy diagram, 2-electrode *J-V* curves]. See DOI: 10.1039/b000000x/

1 X. Chen, L. Liu, Y. Y. Peter and S. S. Mao, *Science*, 2011, **331**, 746.
2 G. Wang, H. Wang, Y. Ling, Y. Tang, X. Yang, R. C. Fitzmorris, C. Wang, J. Z. Zhang and Y. Li, *Nano Lett.*, 2011, **11**, 3026.
3 A. Naldoni, M. Allieta, S. Santangelo, M. Marelli, F. Fabbri, S. Cappelli, C. L. Bianchi, R. Psaro and V. Dal Santo, *J. Am. Chem. Soc.*, 2012, **134**, 7600.
4 Z. Wang, C. Yang, T. Lin, H. Yin, P. Chen, D. Wan, F. Xu, F. Huang, J. Lin and X. Xie, *Adv. Funct. Mater.*, 2013, **23**, 5444.
5 Z. Wang, C. Yang, T. Lin, H. Yin, P. Chen, D. Wan, F. Xu, F. Huang, J. Lin, X. Xie and M. Jiang, *Energy Environ. Sci.*, 2013, **6**, 3007.
6 C. Yang, Z. Wang, T. Lin, H. Yin, X. Lu, D. Wan, T. Xu, C. Zheng, J. Lin, F. Huang, X. Xie and M. Jiang, *J. Am. Chem. Soc.*, 2013, **135**, 17831.
7 X. Yang, A. Wolcott, G. Wang, A. Sobo, R. C. Fitzmorris, F. Qian, J. Z. Zhang and Y. Li, *Nano Lett.*, 2009, **9**, 2331.
8 X. Liu, F. Wang and Q. Wang, *Phys. Chem. Chem. Phys.*, 2012, **14**, 7894.
9 Y. Ling, G. Wang, J. Reddy, C. Wang, J. Z. Zhang and Y. Li, *Angew. Chem. Int. Ed.*, 2012, **51**, 4074.
10 M. Zhou, H. B. Wu, J. Bao, L. Liang, X. W. Lou and Y. Xie, *Angew. Chem. Int. Ed.*, 2013, **52**, 8579.
11 S. Abe, *Nanoscale Res. Lett.*, 2012, **7**, 1.
12 H. Luo, W. Song, P. G. Hoertz, K. Hanson, R. Ghosh, S. Rangan, M. K. Brennaman, J. J. Concepcion, R. A. Binstead and R. A. Bartynski, *Chem. Mater.*, 2012, **25**, 122.
13 A. L. Viet, R. Jose, M. Reddy, B. Chowdari and S. Ramakrishna, *J. Phys. Chem. C*, 2010, **114**, 21795.
14 J. H. Kang, Y. Myung, J. W. Choi, D. M. Jang, C. W. Lee, J. Park and E. H. Cha, *J. Mater. Chem.*, 2012, **22**, 8413.
15 K. Sayama, H. Arakawa and K. Domen, *Catal. Today*, 1996, **28**, 175.
16 H. Zhang, Y. Wang, D. Yang, Y. Li, H. Liu, P. Liu, B. J. Wood and H. Zhao, *Adv. Mater.*, 2012, **24**, 1598.
17 B. Varghese, S. C. Haur and C.-T. Lim, *J. Phys. Chem. C*, 2008, **112**, 10008.
18 H. Liu, N. Gao, M. Liao and X. Fang, *Sci. Rep.*, 2015, **5**, 7716.
19 D. D. Yao, R. A. Rani, A. P. O'Mullane, K. Kalantar-zadeh and J. Z. Ou, *J. Phys. Chem. C*, 2014, **118**, 476.
20 H. Nakazawa, K. Sano, T. Abe, M. Baba and N. Kumagai, *J. Power Sources*, 2007, **174**, 838.
21 O. F. Lopes, E. C. Paris and C. Ribeiro, *Appl. Catal. B*, 2014, **144**, 800.
22 M. Wei, Z.-m. Qi, M. Ichihara and H. Zhou, *Acta Mater.*, 2008, **56**, 2488.
23 H. Wen, Z. Liu, J. Wang, Q. Yang, Y. Li and J. Yu, *Appl. Surf. Sci.*, 2011, **257**, 10084.
24 R. Ghosh, M. K. Brennaman, T. Uher, M. R. Ok, E. T. Samulski, L. E. McNeil, T. J. Meyer and R. Lopez, *ACS Appl. Mater. Interfaces*, 2011, **3**, 3929.
25 A. L. Viet, M. Reddy, R. Jose, B. Chowdari and S. Ramakrishna, *J. Phys. Chem. C*, 2009, **114**, 664.
26 K. Lee, Y. Yang, M. Yang and P. Schmuki, *Chem.- Eur. J.*, 2012, **18**, 9521.
27 R. A. Rani, A. S. Zoolfakar, J. Subbiah, J. Z. Ou and K. Kalantar-zadeh, *Electrochem. Commun.*, 2014, **40**, 20.
28 J. W. Schultze and M. Lohrengel, *Electrochim. Acta*, 2000, **45**, 2499.
29 L. Li, J. Deng, R. Yu, J. Chen, Z. Wang and X. Xing, *J. Mater. Chem. A*, 2013, **1**, 11894.
30 R. A. Rani, A. S. Zoolfakar, A. P. O'Mullane, M. W. Austin and K. Kalantar-Zadeh, *J. Mater. Chem. A*, 2014, **2**, 15683.
31 G. Zhu, T. Lin, X. Lü, W. Zhao, C. Yang, Z. Wang, H. Yin, Z. Liu, F. Huang and J. Lin, *J. Mater. Chem. A*, 2013, **1**, 9650.
32 H. Cui, W. Zhao, C. Yang, H. Yin, T. Lin, Y. Shan, Y. Xie, H. Gu and F. Huang, *J. Mater. Chem. A*, 2014, **2**, 8612.
33 N. Özer, T. Barreto, T. Büyüklimanli and C. M. Lampert, *Sol. Energy Mater. Sol. Cells*, 1995, **36**, 433.
34 T. C. Canevari, L. T. Arenas, R. Landers, R. Custodio and Y. Gushikem, *Analyst*, 2013, **138**, 315.
35 A. Nowak, J. Persson, B. Schmelzer, J. Szade and K. Szot, *J. Phys. D: Appl. Phys.*, 2014, **47**, 135301.
36 S. H. Mujawar, A. I. Inamdar, C. A. Betty, V. Ganesan and P. S. Patil, *Electrochim. Acta*, 2007, **52**, 4899.

37 S. Heusing, D.-L. Sun, J. Otero-Anaya and M. A. Aegerter, *Thin Solid Films*, 2006, **502**, 240.
38 R. Brayner and F. Bozon-Verduraz, *Phys. Chem. Chem. Phys.*, 2003, **5**, 1457.
39 J. M. Jehng and I. E. Wachs, *Chem. Mater.*, 1991, **3**, 100.
40 H. Yin, T. Lin, C. Yang, Z. Wang, G. Zhu, T. Xu, X. Xie, F. Huang and M. Jiang, *Chem.- Eur. J.*, 2013, **19**, 13313.
41 Y. Ling, G. Wang, D. A. Wheeler, J. Z. Zhang and Y. Li, *Nano Lett.*, 2011, **11**, 2119.
42 G. Zhao, H. Kozuka, H. Lin, M. Takahashi and T. Yoko, *Thin Solid Films*, 1999, **340**, 125.
43 C. Mao, F. Zuo, Y. Hou, X. Bu and P. Feng, *Angew. Chem. Int. Ed.*, 2014, **53**, 10485.
44 W. Leng, Z. Zhang, J. Zhang and C. Cao, *J. Phys. Chem. B*, 2005, **109**, 15008.
45 G. Wang, Q. Wang, W. Lu and J. Li, *J. Phys. Chem. B*, 2006, **110**, 22029.
46 E. Gao, W. Wang, M. Shang and J. Xu, *Phys. Chem. Chem. Phys.*, 2011, **13**, 2887.
47 B. H. Meekins and P. V. Kamat, *ACS Nano*, 2009, **3**, 3437.
48 Q. Kang, J. Cao, Y. Zhang, L. Liu, H. Xu and J. Ye, *J. Mater. Chem. A*, 2013, **1**, 5766.
49 T. W. Kim and K. S. Choi, *Science*, 2014, **343**, 990.
50 M. G. Walter, E. L. Warren, J. R. McKone, S. W. Boettcher, Q. Mi, E. A. Santori and N. S. Lewis, *Chem. Rev.*, 2010, **110**, 6446.
51 G. Wang, Y. Ling, H. Wang, X. Yang, C. Wang, J. Z. Zhang and Y. Li, *Energy Environ. Sci.*, 2012, **5**, 6180.

Table of Contents Entry

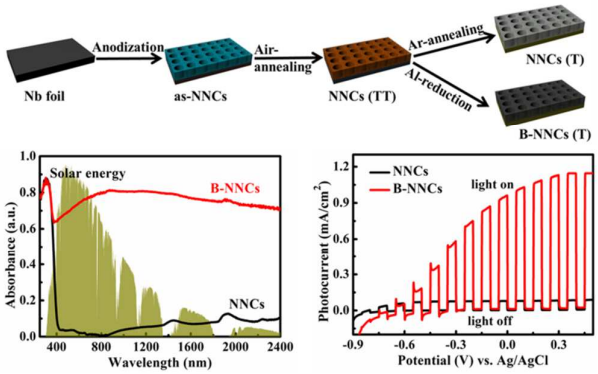

Oxygen-deficient black Nb_2O_5 nanochannels are successfully prepared, and studied as efficient photoanode for photoelectrochemical water splitting for the first time.